Energy and angular distribution of electrons in ionization of He and Ne by 6-MeV/u bare carbon ions: Comparison with continuum-distorted-wave eikonal-initial-state calculations in prior and post forms

Shubhadeep Biswas,[1,*] D. Misra,[1] J. M. Monti,[2] C. A. Tachino,[2] R. D. Rivarola,[2] and L. C. Tribedi[1,†]

[1]*Tata Institute of Fundamental Research, Homi Bhabha Road, Colaba, Mumbai 400 005, India*

[2]*Institute de Fisica Rosario (CONICET-UNR), Universidad Nacional de Rosario, 2000 Rosario, Argentina*

(Received 18 February 2014; revised manuscript received 19 August 2014; published 17 November 2014)

We have measured the absolute double-differential cross sections (DDCS) for electron emission in ionization of He and Ne atoms under the impact of 6-MeV/u C^{6+} ions. Data were collected between 1 and 500 eV for He, while for Ne this range was extended up to 1000 eV. The angular ranges covered in the experiment are 30° to 150° and 20° to 160° for He and Ne, respectively. The DDCS spectra are compared with the prior and the post forms of the state-of-the-art continuum-distorted-wave eikonal-initial-state model. Both the theoretical models show very good agreement with the energy and angular distributions of the DDCS in the case of He. For Ne, at low energies both are going together and matching very well with the data. In the high-energy region, at extreme forward and backward angles, although both the forms are underestimating the experimental data to some extent, the prior form shows much better agreement compared to the post form. This post-prior discrepancy is attributed to the influence of dynamic screening, on the ionized one, produced by the electrons remaining in the target. The single differential cross sections (SDCS) in emission angle ($\frac{d\sigma}{d\Omega_e}$) and electron energy ($\frac{d\sigma}{d\epsilon_e}$) are deduced by integrating the electron DDCS spectra. While excellent agreement is obtained for the $\frac{d\sigma}{d\epsilon_e}$ spectrum, the $\frac{d\sigma}{d\Omega_e}$ provides a further sensitive test to the adequacy of the theoretical model employed. The total cross section obtained from the SDCS spectra is about 11% higher than the prior model for He and about 6% lower for Ne. To get the quantitative picture of the two-center effect, the forward-backward angular asymmetry parameter has been deduced as a function of velocity of the ejected electrons. For both the targets, it is very well reproduced by both the forms of the theory. For the Ne target, *K-LL* Auger angular distribution has also been studied, which shows small asymmetry caused by multiple vacancies in the *L* shell along with the *K*-shell vacancy.

DOI: 10.1103/PhysRevA.90.052714 PACS number(s): 34.50.Fa, 34.50.Gb

I. INTRODUCTION

Electron emission in the ionization of atoms and molecules has been the subject of extensive study from the early days of ion-atom collision investigation. The long-standing interest in this study is due to the ability to reveal microscopic details of the underlying inelastic collision mechanisms. This enables one to explore important features of different processes like soft collision (SE), binary encounter (BE), electron capture to the continuum (ECC), etc. [1]. Kuyatt and Jorgenson, in 1963 [2], first performed the complete measurement of energy and angular distributions of electron emission in ionization of H_2 under keV energy proton impact. In most of the earlier cases double-differential cross sections (DDCS) have been measured for simple targets like H [3,4], H_2 [3,5–11], and He [3,12–16]. In the case of multielectronic systems, the process of collision-induced electron emission is much more complicated due to the presence of many electrons.

In the late 1970s, it has been realized that in the case of highly charged ions, postcollision trajectories of the electrons emitted in target ionization are governed by both the target as well as the projectile Coulomb fields. Such a two-center effect (TCE) results in an asymmetry in angular distribution of electron emission. From previous works [3,14,15], it is well established that, for highly charged projectiles first-order Born (B1) calculation fails to describe the experimental data even if the projectile velocity is very high. This is because B1 calculation mainly takes into account the target center effects. To incorporate the projectile influence on the active electron in the entrance and exit channels of the collision, Crothers and McCann [17] developed a theoretical model based on continuum-distorted-wave eikonal-initial-state (CDW-EIS) approximation following the works of Cheshire [18] (CDW for electron capture) and Belkić [19] (CDW for ionization). This perturbative model has been extremely successful in producing the existing experimental results for low-*Z* targets. Over time, this model has been extended for multielectronic systems [20], which was a big step forward towards the understanding of the collision mechanisms for the multielectronic targets. In multielectronic systems, due to the additional passive electrons (the nonionized ones) the interaction potential no longer remains Coulombic in nature, and its influence on the dynamical evolution of the ionized electron must be considered. Moreover, the deviation of the target potential from the pure Coulomb potential contributes to angular asymmetry along with the TCE [21]. All these complications due to the target non-Coulomb potential are also very hard to be incorporated in any *ab initio* calculation. In this regard it should be mentioned that there are many fruitful references to the nonperturbative models [22–27] and the density-functional theories [28–30], which have been sufficiently effective to tackle the multielectronic problem particularly for the heavier atomic targets, large molecules, clusters or even solids.

*shubhadeep@tifr.res.in

†lokesh@tifr.res.in

To have a comprehensive understanding of the electron emission mechanism in the case of multielectronic systems, an appreciable amount of data sets is needed involving multielectronic targets. In this respect, atoms are a more suitable choice than the molecules because of their molecular nature which introduces additional complications in the analysis. It is worth mentioning that the elaborate experimental data sets of e-DDCS for the Ne target in wide angular and energy ranges are not available for too many cases. In most of the earlier cases keV energy low charge state ions like H^+ [31–36] or He^+ [37] or He^{2+} [31,32,35,36] were used for such studies with Ne as the target. In very few cases low charged dressed Ne ions [38,39] of keV energy were used as the projectile. To the best of our knowledge, there is no study of ionization of Ne atoms involving MeV/u energy highly charged bare ions. It should be mentioned here that in the MeV energy range Coulomb ionization is the dominant process; other second-order processes (electron capture to projectile, transfer ionization, etc.) have an increasing role with decreasing impact energy. Thus, the experimental study involving MeV energy heavy bare ions and Ne as the target can give a stringent test to the CDW-EIS model for multielectronic atoms. It enables us to understand the influence of additional passive electrons over the ionization process of the target active electron. In this context, it should be mentioned here that the high-resolution recoil-ion momentum spectroscopy (RIMS) technique, which provides the cross sections differential in the longitudinal and transverse momentum of all the particles in the final state, is proved to be another very powerful tool to disclose several new facts regarding the ionization dynamics in atomic collisions using electrons, ions or photons as projectiles [40–46]. The relation between recoil-ion momentum spectroscopy and continuum electron spectroscopy techniques was also addressed before [5,47,48].

In this report, we expose a detailed measurement of doubly differential distributions of electrons emitted in the ionization of Ne atoms under 6-MeV/u C^{6+} ion impact. In addition, for elaborate comparison, we also discuss the detailed DDCS distribution of electron emission from ionization of He under same projectile impact. This comparison enables us to understand the difference between ionization mechanisms of low-Z and high-Z target atoms. Additionally, it would contribute to the process of building a wider data base for ion-atom collisions, which helps to proceed towards a better understanding of the mechanisms of two-center electron emission. We measure the ejected electron DDCS in the energy range between 1 and 1000 eV, at 12 different angles ranging between 20° and 160° for Ne. For He, the measurements are done in the 1–500 eV energy range at nine different angles between 30° and 150°. Experimentally obtained differential cross sections have been compared with both the prior and the post forms of the state-of-the-art continuum-distorted-wave eikonal-initial-state (CDW-EIS) model. In addition, we report a detailed discussion on the forward-backward asymmetry parameter derived from DDCS energy and angular distributions. For Ne, the Auger electron angular distribution is also discussed in detail. The absolute DDCS data for both He and Ne are also provided in tabular form for ready reference.

II. OVERVIEW OF THE EXPERIMENT

The present experiments were carried out with 6-MeV/u C^{6+} ions available from the 14 MV BARC-TIFR Pelletron accelerator facility in Mumbai, India. Energy and the charge state of the ion beam were analyzed by the dipole and switching magnets, installed at different positions of the accelerator. The beam was then collimated into the desired size using a pair of four-jaw slits (2×2 mm^2) mounted 1 m apart along the beamline followed by another aperture of 4-mm diameter. Finally, the well-collimated beam was passed through a differential pumping arrangement followed by the interaction chamber. During the experiment base pressure of the scattering chamber was maintained better than 2×10^{-7} Torr. For taking data with target gas, the scattering chamber was flooded with He at an absolute pressure of 0.2 mTorr for lower energy ($\lesssim$100 eV) data and with 0.3 mTorr for higher energies. For Ne, 0.15-mTorr pressure was maintained for the entire data accumulation. The absolute pressure, on top of the chamber base vacuum, was measured by the capacitance manometer (MKS Baratron). To get the absolute cross section, background subtraction was done by taking data in without the gas condition keeping the rest of the parameters unaltered. The secondary electrons emitted in the collision process were energy analyzed by a hemispherical electrostatic energy analyzer of energy resolution 6% [49]. These energy analyzed electrons were then detected by a channel electron multiplier (CEM) kept at the exit of the analyzer. For each angle, electrons of different energies were detected for a certain number of incident projectiles that were collected on a Faraday cup. To detect the low-energy electrons which are vulnerable to Earth's magnetic field, two sets of thin μ-metal sheets were lined inside the scattering chamber. This reduces the magnetic field at about 5–10 mGauss near the interaction region. Proper cleanness was maintained to get rid of the stray electric fields which would deviate the secondary electrons from their proper path. To check the alignment of the chamber, two DDCS spectra were taken at two 90° (±90°) positions with respect to the projectile beam and those two values match well (within 7%–8%) with each other [see Fig. 1(d)].This indicates a good alignment of the spectrometer with respect to the direction of the projectile beam. From the measured electron spectrum at a given angle, double-differential cross sections were obtained from the first principle [49]. For He, DDCS spectra were taken for nine different angles, i.e., 30°, 45°, 60°, 75°, 90°, 105°, 120°, 135°, and 150°, whereas for Ne the same measurements were done for 12 different angles, i.e., 20°, 30°, 45°, 60°, 75°, 80°, 90°, 105°, 120°, 135°, 150°, and 160°. At each angle, the ejected electrons having energies between 1 and 500 eV were detected for He. The observation of the autoionization peak at 35.5 eV in the He spectrum makes sure about the energy calibration of the spectrometer. For Ne, the energy range was extended up to 1000 eV in order to detect the *K-LL* Auger electrons at around 780 eV. Some of the representative values of absolute electron DDCS are tabulated in Table I (He) and Table II (Ne).

The estimated error due to the statistical fluctuation was low ($\leqslant$7%) throughout the whole energy range, for forward and intermediate angles, for both the targets. It increases to around 20%–30% for extreme backward angles especially for the high energy (above 350 eV for He and 600 eV for Ne) electrons.

TABLE I. Measured double-differential cross sections for He in units of Mb/(eV sr) at different angles. Last column displays the $\frac{d\sigma}{d\epsilon_e}$ values in units of Mb/eV. Last row displays the $\frac{d\sigma}{d\Omega_e}$ values in units of Mb/sr. For errors, see the text. Bracket notation is power-of-ten notation, i.e., 7.54[−1] means 7.54×10^{-1}.

ϵ_e (eV)	30°	45°	60°	75°	90°	105°	120°	135°	150°	$\frac{d\sigma}{d\epsilon_e}$
1	7.54[−1]	7.79[−1]	1.10[0]	9.32[−1]	9.07[−1]	8.99[−1]	8.55[−1]	5.16[−1]	5.02[−1]	9.39[0]
3	6.48[−1]	6.96[−1]	1.06[0]	7.99[−1]	7.60[−1]	7.34[−1]	6.49[−1]	4.09[−1]	3.48[−1]	7.98[0]
7	4.74[−1]	5.32[−1]	8.26[−1]	5.91[−1]	5.54[−1]	5.69[−1]	4.43[−1]	2.45[−1]	2.05[−1]	5.88[0]
11	3.71[−1]	4.11[−1]	6.20[−1]	4.61[−1]	4.28[−1]	4.21[−1]	2.94[−1]	1.69[−1]	1.36[−1]	4.39[0]
15	2.72[−1]	2.97[−1]	4.73[−1]	3.79[−1]	3.54[−1]	3.10[−1]	2.07[−1]	1.16[−1]	9.68[−2]	3.35[0]
21	1.94[−1]	2.00[−1]	3.22[−1]	2.87[−1]	2.56[−1]	2.12[−1]	1.32[−1]	7.47[−2]	6.31[−2]	2.34[0]
31	1.17[−1]	1.25[−1]	1.95[−1]	1.85[−1]	1.70[−1]	1.27[−1]	7.08[−2]	4.06[−2]	3.55[−2]	1.43[0]
41	7.27[−2]	7.52[−2]	1.28[−1]	1.30[−1]	1.19[−1]	7.85[−2]	4.11[−2]	2.20[−2]	1.85[−2]	9.40[−1]
50	4.49[−2]	5.06[−2]	9.62[−2]	9.48[−2]	8.72[−2]	5.43[−2]	2.38[−2]	1.28[−2]	1.06[−2]	6.48[−1]
60	2.73[−2]	3.76[−2]	6.05[−2]	7.74[−2]	6.87[−2]	3.90[−2]	1.55[−2]	9.13[−3]	7.45[−3]	4.84[−1]
70	1.81[−2]	2.52[−2]	5.30[−2]	5.95[−2]	5.30[−2]	2.58[−2]	9.78[−3]	5.50[−3]	4.57[−3]	3.57[−1]
80	1.38[−2]	1.98[−2]	3.50[−2]	4.94[−2]	4.39[−2]	2.03[−2]	7.28[−3]	4.07[−3]	3.33[−3]	2.84[−1]
90	1.03[−2]	1.45[−2]	3.10[−2]	3.92[−2]	3.48[−2]	1.48[−2]	4.80[−3]	2.65[−3]	2.10[−3]	2.19[−1]
100	8.12[−3]	1.20[−2]	2.08[−2]	3.40[−2]	3.02[−2]	1.19[−2]	3.61[−3]	2.04[−3]	1.72[−3]	1.81[−1]
120	5.13[−3]	7.81[−3]	1.55[−2]	2.51[−2]	2.27[−2]	7.40[−3]	2.03[−3]	1.14[−3]	1.07[−3]	1.29[−1]
140	3.48[−3]	4.88[−3]	1.09[−2]	1.89[−2]	1.74[−2]	5.00[−3]	1.34[−3]	7.05[−4]	5.98[−4]	9.40[−2]
160	2.20[−3]	3.15[−3]	7.64[−3]	1.54[−2]	1.33[−2]	3.43[−3]	8.83[−4]	4.33[−4]	3.81[−4]	7.04[−2]
200	1.20[−3]	1.91[−3]	4.57[−3]	1.04[−2]	8.68[−3]	1.47[−3]	4.23[−4]	1.72[−4]	1.69[−4]	4.39[−2]
250	6.50[−4]	8.89[−4]	2.68[−3]	7.56[−3]	5.21[−3]	7.53[−4]	1.74[−4]	7.49[−5]	7.44[−5]	2.77[−2]
300	3.43[−4]	5.58[−4]	1.73[−3]	5.71[−3]	3.35[−3]	3.61[−4]	7.03[−5]	4.71[−5]	4.10[−5]	1.88[−2]
350	1.90[−4]	3.24[−4]	1.35[−3]	4.73E-3	2.20[−3]	1.71[−4]	4.11[−5]	1.83[−5]	1.77[−5]	1.41[−2]
400	1.31[−4]	2.30[−4]	9.72[−4]	3.63[−3]	1.60[−3]	9.39[−5]	2.05[−5]	1.62[−5]	1.54[−5]	1.05[−2]
450	7.83[−5]	1.50[−4]	6.88[−4]	3.28[−3]	1.04[−3]	6.04[−5]	1.29[−5]	8.70[−6]	8.47[−6]	8.35[−3]
500	5.84[−5]	9.71[−5]	4.98[−4]	2.94[−3]	7.66[−4]	4.07[−5]	6.97[−6]	4.40[−6]	4.87[−6]	6.94[−3]
$\frac{d\sigma}{d\Omega_e}$	1.23[1]	1.37[1]	1.91[1]	2.14[1]	1.92[1]	1.43[1]	8.63[0]	5.52[0]	4.77[0]	

But measurements in the Auger region for Ne carry relatively low uncertainty. The quoted statistical errors are estimated after proper background subtraction. In Figs. 1(a)–1(c), the typical ratio between data and background electron counts are shown for three different angles for Ne. Apart from the statistical uncertainty, the main contribution to the absolute error is from the gas pressure, which is about 6%–7%. The other uncertainties, together, contribute very less ($\backsim$1.5%), which are mainly arising from observation angle and solid angle measurements. It should be mentioned here that the CEM efficiency correction has also been done to get the DDCS values.

III. THEORETICAL MODELS

Let us consider the single ionization reaction of a multielectronic atom. The incident particle is a bare ion of charge Z_P that impinges on the atomic target with velocity $\vec{v}$ parallel to the z axis of a laboratory reference frame located at the target nucleus. The multielectronic problem is reduced to the analysis of the one-electron system in which the passive electrons (the nonionized ones) are considered to remain frozen in their initial orbitals during the collision, whereas the active electron (the emitted one) evolves in a mean field of the residual target [20].

Into the straight line version of the impact parameter approximation, if contributions coming from all projectile scattering angles are added, double-differential cross sections as a function of the energy ε_k and the solid angle Ω_k of the emitted electron can be defined as follows:

$$\sigma^{(2)}(\varepsilon_k,\theta_k) = \frac{d\sigma}{d\varepsilon_k\, d\Omega_k} = k \int d\vec{\rho}\, |a_{if}^{\pm}(\vec{\rho})|^2, \qquad (1)$$

where the sign + (−) refers to the post (prior) version of the transition amplitude $a_{if}(\vec{\rho})$, $k = |\vec{k}|$ with $\vec{k}$ the momentum of the emitted electron, and $\vec{\rho}$ the impact parameter vector.

Within the distorted-wave model, the first-order approximation for the post and prior versions of the transition amplitude for the active electron may be written as

$$a_{if}^{+}(\vec{\rho}) = -i \int_{-\infty}^{+\infty} dt\, \langle \chi_f^{-} | \left(H - i\frac{\partial}{\partial t} \right)^{\dagger} | \chi_i^{+} \rangle \qquad (2)$$

and

$$a_{if}^{-}(\vec{\rho}) = -i \int_{-\infty}^{+\infty} dt\, \langle \chi_f^{-} | \left(H - i\frac{\partial}{\partial t} \right) | \chi_i^{+} \rangle, \qquad (3)$$

respectively. In Eqs. (2) and (3), χ_i^{+} and χ_f^{-} are distorted wave functions that satisfy correct outgoing and incoming asymptotic boundary conditions, respectively, and H is the active-electron Hamiltonian,

$$H = -\frac{\nabla_x^2}{2} - V_T(\vec{x}) - \frac{Z_P}{s} = -\frac{\nabla_x^2}{2} - \frac{Z_T}{x} - V_{ap}(\vec{x}) - \frac{Z_P}{s}, \qquad (4)$$

TABLE II. Measured double-differential cross sections for Ne in units of Mb/(eV sr) at different angles. Last column displays the $\frac{d\sigma}{d\epsilon_e}$ values in units of Mb/eV. Last row displays the $\frac{d\sigma}{d\Omega_e}$ values in units of Mb/sr. For errors, see the text. Bracket notation is power-of-ten notation, i.e., 8.17[−1] means 8.17×10^{-1}.

ϵ_e (eV)	20°	30°	45°	60°	75°	80°	90°	105°	120°	135°	150°	160°	$\frac{d\sigma}{d\epsilon_e}$
1	3.28[0]	2.88[0]	3.44[0]	3.09[0]	3.00[0]	2.80[0]	2.75[0]	2.68[0]	2.67[0]	2.56[0]	2.38[0]	2.31[0]	3.36[1]
3	2.49[0]	2.04[0]	2.46[0]	2.36[0]	2.34[0]	2.20[0]	2.15[0]	2.05[0]	2.04[0]	1.94[0]	1.80[0]	1.66[0]	2.59E1
7	1.49[0]	1.39[0]	1.80[0]	1.54[0]	1.63[0]	1.49[0]	1.45[0]	1.42[0]	1.33[0]	1.18[0]	1.22[0]	9.43[−1]	1.71[1]
11	1.01[0]	1.04[0]	1.25[0]	1.13[0]	1.20[0]	1.09[0]	1.07[0]	9.75[−1]	8.68[−1]	7.33[−1]	7.21[−1]	5.53[−1]	1.18[1]
15	8.17[−1]	8.23[−1]	8.90[−1]	8.80[−1]	9.30[−1]	8.49[−1]	8.29[−1]	7.77[−1]	6.74[−1]	5.18[−1]	5.26[−1]	3.89[−1]	9.05[0]
21	6.26[−1]	6.10[−1]	6.09[−1]	6.87[−1]	6.84[−1]	6.39[−1]	6.07[−1]	5.41[−1]	5.11[−1]	3.66[−1]	3.64[−1]	2.50[−1]	6.60[0]
30	4.11[−1]	4.07[−1]	4.45[−1]	4.80[−1]	4.81[−1]	4.52[−1]	4.24[−1]	3.72[−1]	3.30[−1]	2.68[−1]	1.98[−1]	1.65[−1]	4.55[0]
40	2.93[−1]	2.82[−1]	3.09[−1]	3.59[−1]	3.61[−1]	3.39[−1]	3.17[−1]	2.64[−1]	2.30[−1]	1.76[−1]	1.38[−1]	1.02[−1]	3.28[0]
50	2.12[−1]	2.06[−1]	2.40[−1]	2.69[−1]	2.80[−1]	2.64[−1]	2.38[−1]	2.01[−1]	1.53[−1]	1.22[−1]	9.17[−2]	6.86[−2]	2.44[0]
60	1.60[−1]	1.58[−1]	1.88[−1]	2.06[−1]	2.17[−1]	2.19[−1]	1.89[−1]	1.50[−1]	1.16[−1]	8.18[−2]	5.89[−2]	4.80[−2]	1.86[0]
70	1.22[−2]	1.23[−1]	1.44[−1]	1.64[−1]	1.78[−1]	1.72[−1]	1.45[−1]	1.14[−1]	8.17[−2]	5.97[−2]	4.49[−2]	3.52[−2]	1.44[0]
80	9.77[−2]	9.84[−2]	1.19[−1]	1.35[−1]	1.36[−1]	1.34[−1]	1.20[−1]	9.03[−2]	6.05[−2]	4.50[−2]	3.37[−2]	2.44[−2]	1.14[0]
90	7.86[−2]	8.05[−2]	8.82[−2]	1.12E-1	1.20E-1	1.17E-1	9.54[−2]	7.06[−2]	4.70[−2]	3.52[−2]	2.46[−2]	1.80[−2]	9.24[−1]
100	6.62[−2]	6.70[−2]	7.49[−2]	9.50[−2]	9.65[−2]	9.85[−2]	8.37[−2]	6.07[−2]	3.62[−2]	2.49[−2]	1.97[−2]	1.34[−2]	7.71[−1]
120	4.63[−2]	4.55[−2]	5.56[−2]	7.17[−2]	7.36[−2]	7.21[−2]	6.40[−2]	3.75[−2]	2.32[−2]	1.63[−2]	1.19[−2]	8.50E-3	5.52[−1]
140	3.49[−2]	3.32[−2]	3.98[−2]	5.24[−2]	5.95[−2]	5.68[−2]	5.57[−2]	2.94[−2]	1.62[−2]	9.94[−3]	7.51[−3]	5.17[−3]	4.23[−1]
160	2.53[−2]	2.56[−2]	3.00[−2]	3.94[−2]	4.37[−2]	4.72[−2]	3.54[−2]	2.16[−2]	1.03[−2]	7.08[−3]	4.72[−3]	4.16[−3]	3.07[−1]
200	1.58[−2]	1.56[−2]	1.96[−2]	2.45[−2]	3.24[−2]	3.21[−2]	2.48[−2]	1.30[−2]	6.29[−3]	3.54[−3]	3.45[−3]	2.40[−3]	2.02[−1]
240	1.10[−2]	1.03[−2]	1.26[−2]	1.74[−2]	2.47[−2]	2.37[−2]	1.74[−2]	8.25[−3]	3.85[−3]	2.35[−3]	2.29[−3]	1.41[−3]	1.41[−1]
280	7.91[−3]	7.34[−3]	8.97[−3]	1.28[−2]	1.78[−2]	1.77[−2]	1.28[−2]	5.71[−3]	2.14[−3]	1.24[−3]	1.47[−3]	8.78E-4	1.01[−1]
320	5.48[−3]	5.63[−3]	6.43[−3]	9.09[−3]	1.45[−2]	1.46[−2]	9.23[−3]	3.75[−3]	1.36[−3]	8.20[−4]	7.01[−4]	7.02[−4]	7.47[−2]
360	4.74[−3]	3.99[−3]	5.16[−3]	7.35[−3]	1.22[−2]	1.15[−2]	8.04[−3]	2.69[−3]	1.06[−3]	6.58[−4]	6.34[−4]	5.11[−4]	6.04[−2]
400	3.89[−3]	3.29[−3]	3.91[−3]	5.87[−3]	1.08[−2]	1.01[−2]	5.34[−3]	2.08[−3]	7.96[−4]	4.51[−4]	4.30[−4]	3.51[−4]	4.82[−2]
440	2.87[−3]	2.77[−3]	3.17[−3]	4.87[−3]	8.98[−3]	8.05[−3]	4.11[−3]	1.24[−3]	7.08[−4]	3.21[−4]	3.64[−4]	2.68[−4]	3.84[−2]
480	2.38[−3]	2.12[−3]	2.45[−3]	4.21[−3]	7.56[−3]	6.87[−3]	3.62[−3]	1.07[−3]	5.45[−4]	3.41[−4]	2.25[−4]	2.05[−4]	3.23[−2]
520	2.10[−3]	1.72[−3]	2.17[−3]	3.25[−3]	6.79[−3]	6.32[−3]	2.96[−3]	8.43[−4]	4.44[−4]	2.67[−4]	1.65[−4]	1.80[−4]	2.75[−2]
560	1.70[−3]	1.59[−3]	1.87[−3]	3.25[−3]	6.35[−3]	5.25[−3]	2.24[−3]	6.86[−4]	3.09[−4]	1.95[−4]	1.56[−4]	1.43[−4]	2.42[−2]
600	1.53[−3]	1.45[−3]	1.57[−3]	2.82[−3]	5.87[−3]	4.47[−3]	1.96[−3]	5.39[−4]	2.43[−4]	1.67[−4]	1.28[−4]	9.87[−5]	2.12[−2]
$\frac{d\sigma}{d\Omega_e}$	4.65[1]	4.61[1]	4.80[1]	5.40[1]	5.79[1]	5.54[1]	4.79[1]	4.33[1]	3.63[1]	2.92[1]	2.63[1]	2.46[1]	

with $V_{ap}(\vec{x})$ the interaction of the active electron with all the passive ones averaged on their initial distributions:

$$V_{ap}(\vec{x}) = \langle\varphi_p(\{\vec{x}_p\})|\sum_p \frac{1}{|\vec{x}-\vec{x}_p|}|\varphi_p(\{\vec{x}_p\})\rangle. \quad (5)$$

In the preceding expressions, $\{\vec{x}_p\}$ represents the ensemble of the passive electron positions $\vec{x}_p$ and $\varphi_p(\{\vec{x}_p\})$ is the passive electron wave function. In addition, $\vec{x}$ is the electron coordinate with respect to the laboratory reference frame, and $\vec{s}$ is the electron position vector with respect to the projectile nucleus.

In the continuum-distorted-wave eikonal-initial-state (CDW-EIS) approximation [17], χ_i^+ and χ_f^- are chosen as

$$\chi_i^{+,\mathrm{EIS}}(\vec{x},t) = \varphi_i(\vec{x})\exp(-i\varepsilon_i t)\,\mathcal{L}_i^{+,\mathrm{EIS}}(\vec{s}) \quad (6)$$

$$\chi_f^{-,\mathrm{CDW}}(\vec{x},t) = \varphi_k(\vec{x})\exp(-i\varepsilon_k t)\,\mathcal{L}_f^{-,\mathrm{CDW}](\vec{s})}, \quad (7)$$

with φ_i and φ_k the bound and continuum wave functions of the active electron, respectively, ε_i is the initial orbital energy, and $\varepsilon_k = k^2/2$. The initial and final distorting functions $\mathcal{L}_i^{+,\mathrm{EIS}}(\vec{s})$ and $\mathcal{L}_f^{-,\mathrm{CDW}}(\vec{s})$ are given by the projectile eikonal and continuum factors:

$$\mathcal{L}_i^{+,\mathrm{EIS}}(\vec{s}) = \exp[-i\nu\ln(vs+\vec{v}\cdot\vec{s})], \quad (8)$$

$$\mathcal{L}_f^{-,\mathrm{CDW}}(\vec{s}) = N(\varsigma)\,{}_1F_1[-i\varsigma;1;-i(ps+\vec{p}\cdot\vec{s})], \quad (9)$$

respectively, where $\nu = Z_P/v$, $\varsigma = Z_P/p$ with $\vec{p} = \vec{k}-\vec{v}$ the momentum of the electron considered with respect to a reference frame fixed on the projectile nucleus, and $N(a) = \exp(a\pi/2)\,\Gamma(1+i\,a)$, with ${}_1F_1(b;c;z)$ the Kummer confluent hypergeometric function.

Initial bound orbitals are described by Roothaan-Hartree-Fock (RHF) wave functions [50]. In order to facilitate the calculations, usually the active electron-residual target potential in the exit channel is approximated by a Coulomb potential:

$$V_T(\vec{x}) \approx -\frac{Z_T^*}{x}, \quad (10)$$

with Z_T^* being an effective nuclear charge. Moreover, in expression (2), a residual perturbative potential,

$$V_r(\vec{x}) = -\frac{(Z_T - Z_T^*)}{x} + V_{ap}(\vec{x}), \quad (11)$$

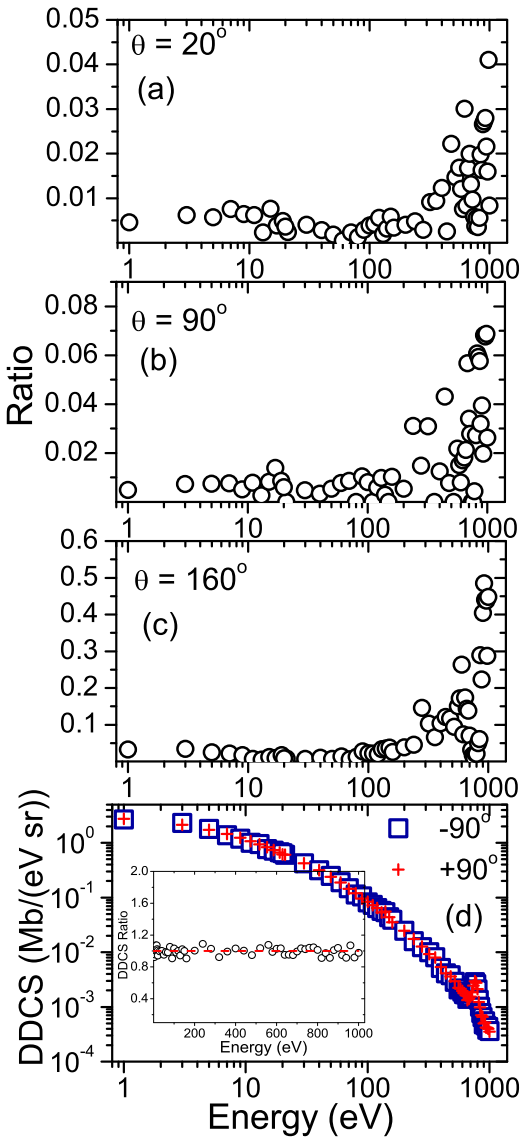

FIG. 1. (Color online) (a)–(c) Energy distribution of the ratio of the electron count corresponding to background (without target gas) and target gas (Ne), at different observation angles. (d) Absolute DDCS corresponding to $+90^\circ$ (circle) and -90° (square). (Inset) Ratio of the corresponding DDCSs.

is neglected. This term contains the influence of the passive electron on the dynamical evolution of the active one, which is only partially taken into account in the potential $-Z_T^*/x$ [51,52]. Thus, the continuum state of the emitted electron is written as

$$\varphi_k(\vec{x}) = (2\pi)^{-3/2}\, \exp(i\,\vec{k}\cdot\vec{x})\, N(\xi)\, {}_1F_1 \times (-i\,\xi; 1; -i\,k\,x - i\,\vec{k}\cdot\vec{x}). \qquad (12)$$

In Eq. (12), $\xi = Z_T^*/k$, being Z_T^* defined following the same criteria employed by Belkić for electron capture [19], namely $Z_T^* = \sqrt{-2\,n_i^2\,\varepsilon_i}$, where n_i is the principal quantum number of each atomic orbital that can be occupied by the active electron. Then, a sum on all atomic orbital contributions is done.

The neglect of the residual potential (11) in the post form [see Eq. (2)] of the scattering amplitude, which explicitly appears as an additional perturbative term, introduces discrepancies in the double-differential cross sections obtained using this form or the prior one. In the prior version the influence of the passive electrons on the active one given by Eq. (5) is included in good approximation in the initial channel considering that electron radial correlation is taken into account when RHF wave functions are employed. Thus, this interaction does not appear as a perturbative term like in the post version [see Eq. (3)]. Moreover, it has been shown that when the non-Coulombic potential (11) is included in the post form calculations, post-prior discrepancies vanish (see especially [52] and also [51,53]). Thus, differences in the post (which is the commonly used version) and prior predictions give a first-order estimation of the influence in the final channel of the passive electrons on the dynamical evolution of the ejected one. The corresponding effect is known as *dynamic screening* [51].

IV. RESULTS AND DISCUSSIONS

A. Energy distributions of the electron DDCS at fixed emission angle

The measured energy distributions of the absolute DDCS of electron emission from the ionization of He and Ne atoms are shown in Figs. 2 and 3, respectively, for different observation angles. As can be seen from both the figures, the cross section reaches maximum at the lowest energy end of the spectrum, which can be attributed to the soft collision electrons (SE). These electrons, which contribute the most to the total cross section, are produced in high-impact parameter collisions involving low momentum transfer. After the SE peak, the DDCS decreases by several orders of magnitude with the increase of electron energy. The electrons emitted with energies more than a few tens of eV up to the end of the spectrum correspond to the so-called two-center electron-emission (TCEE) process, although there is no clear border line from which TCEE starts. For He (Fig. 2), the data have been taken up to 5500 eV in case of 60°. It clearly shows a very broad peak around 3500 eV [Fig. 2(c) inset]. This peak is produced by the binary encounter (BE) collision mechanism.

In the spectrum for Ne (Fig. 3), each of the plots has a sharp peak at 780 eV (inset). These peaks correspond to the *K-LL* Auger electron emission for Ne. These peaks also have some width. The broadness of the peak is due to the fact that this is not a single Auger line, but an admixture of multiple satellite Auger lines. These satellite lines arise due to different *L*-subshell vacancies of the target atom during the collision. The full width at half maximum (FWHM) of the Auger transition peak, at different emission angles, turns out to be approximately 15% of the characteristic Auger transition energy. A careful observation to the Auger peaks suggests that it is more prominent at the backward angles ($\theta \geqslant 105^\circ$) compared to the forward and the intermediate angles. This is because the cross sections due to the Coulomb ionization continuum is relatively low in the backward angles, whereas the *K-LL* Auger distribution is nearly isotropic in nature. If we compare between He and Ne data, the overall cross section is

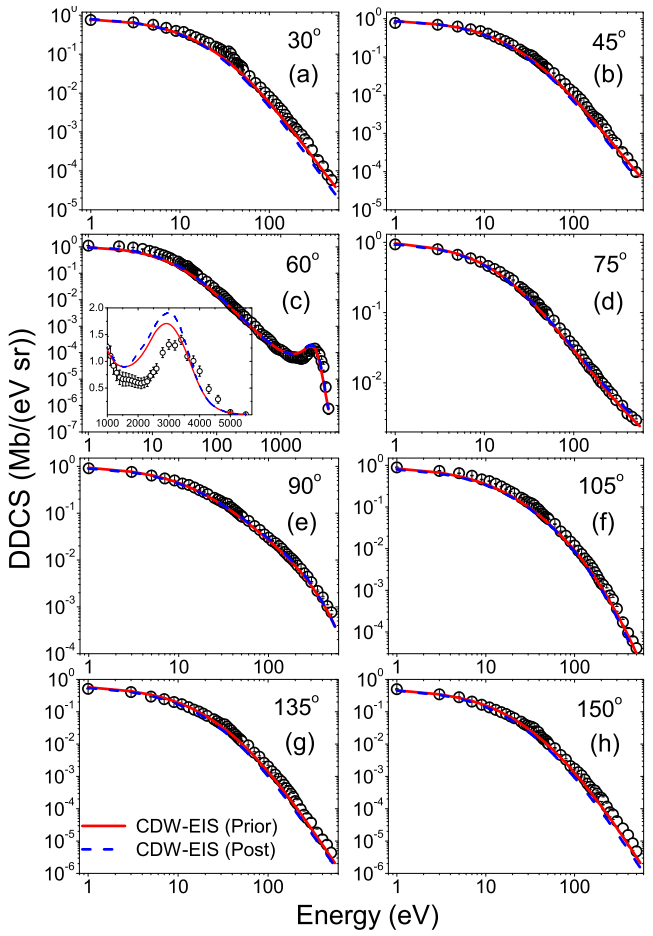

FIG. 2. (Color online) Energy distribution of DDCS at different emission angles for He. Solid (dash) lines represent CDW-EIS prior (post) form. In the inset (c), the BE region at 60° is displayed. The vertical scale of the inset is to be multiplied by 10^{-5}.

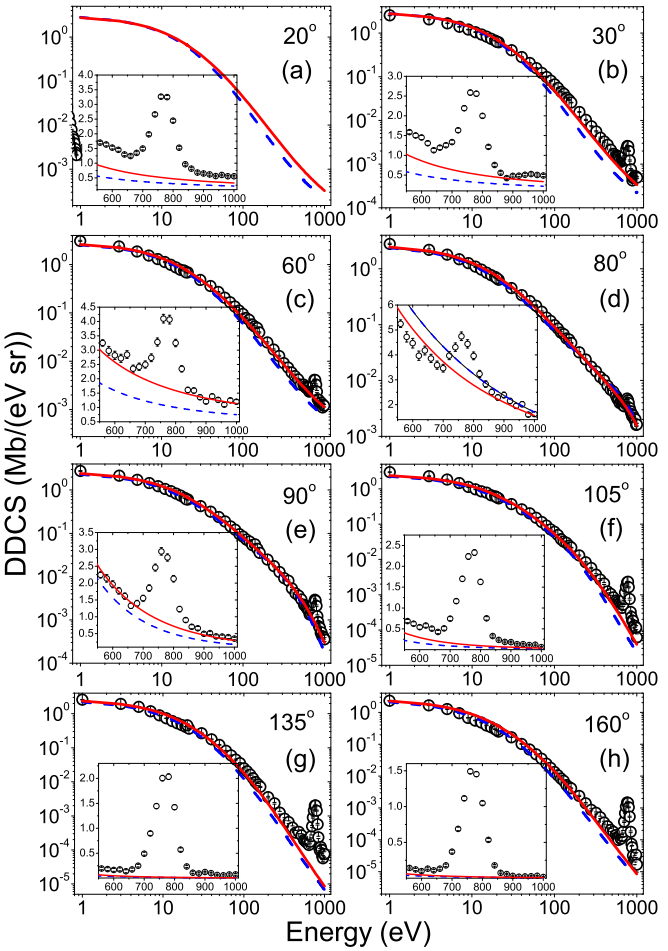

FIG. 3. (Color online) The same as Fig. 2 for the Ne target. In the insets the Auger region is displayed. The vertical scales of the insets are to be multiplied by 10^{-4}.

higher in the case of Ne. This may be because of the higher number of electrons available for ionization and due to the difference in binding energies (The first ionization potentials of He and Ne are 24.6 and 21.6 eV, respectively).

The experimental DDCS data have been compared with the theoretical calculations based on the CDW-EIS model. Calculations have been performed in both, the prior (solid line) as well as the post (dash line) versions of the model. In the post version we have neglected the residual potential given by Eq. (11) in order to estimate the role played by the corresponding dynamic screening on the DDCS. In general, a qualitative good agreement among the experimental data and both the forms of the theory has been obtained, for different emission angles, for both the targets. In case of the He target (Fig. 2), the difference between the post and the prior forms is hardly visible especially for the intermediate angels. In extreme forward and backward angles, a small difference is noticeable in the high energies ($\gtrsim$ 100 eV), where the post form is going slightly below the prior form. As far as absolute agreement between theory and data is concerned, for all angles prior calculation is matching very well with the experiment. In the case of the BE peak at 60° for He [see inset of Fig. 2(c)], a close inspection suggests that the peak position as suggested by both forms of the theory is at slightly lower energy (∼3000 eV) compared to the experimental observation (∼3500 eV). The theories are also overestimating the peak width and the differential cross section as obtained from the experiment. Overall, there is a discrepancy between theory and experiment at the rising edge of the BE peak.

For the Ne target (Fig. 3), there is a clear visible difference between both the forms at high energies ($\gtrsim$ 100 eV), for all angles except 80° and 90°. The agreement with the experiment is much better in case of the prior version calculation (solid line) compared to the post version (dash line), for all angles. For example, at 30°, the DDCS value at 400 eV is underestimated by prior form by a factor of 1.6, whereas it is underestimated by post form by a factor of 3.0. At 135°, these values are 2.0 and 3.2, respectively. As energy increases, this difference between the prior and the post forms keeps increasing.

The above mentioned facts are much more clearly visible from Fig. 4, where the experimental data have been divided by both the theoretical models and plotted against electron energy. It is evident that, in general, the deviation of both the forms of the theoretical calculation from the experimental data is more in the case of Ne compared to that for He. On the other hand, the better agreement of the prior form compared to

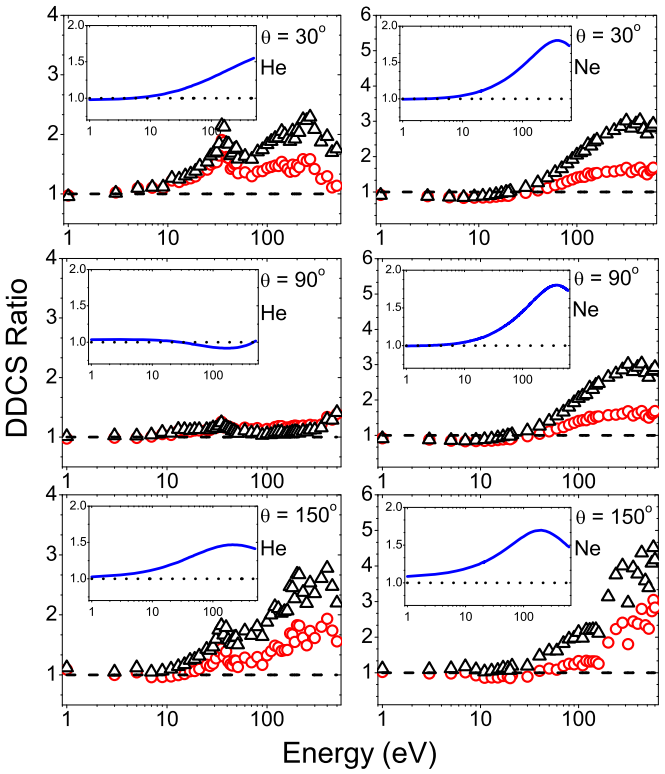

FIG. 4. (Color online) Energy distributions of the ratio corresponding to the DDCS from experiment with the prior (post) form displayed as a circle (triangle). (Insets) DDCS corresponding to prior and post forms. Dash line is ratio = 1.0.

the post form indicates the importance of dynamic screening introduced by the target passive electrons. Larger discrepancy in the case of Ne also supports this fact, as it has more passive electrons. Larger deviation in the backward angles compared to the forward angles for both the targets may be because of the backscattered electrons, which are considered to be much more influenced by the target residual electron cloud. Therefore, the dynamic screening part plays a comparatively bigger role for those electrons. The remaining discrepancy with the experiment may be attributed to the way that the two-center description of the final continuum state is chosen in the CDW-EIS formalism.

B. DDCS angular distributions at fixed electron energy

A qualitatively good agreement has been observed between the CDW-EIS model and the experimental data regarding the energy distribution of the DDCS. Since the DDCS falls over 5–6 orders of magnitude over the ejected electron energy of 1–1000 eV, it is difficult to estimate the small deviations from the model calculations. In that sense, the angular distribution of the measured DDCS provides a clearer picture, exploring the deviations better. Figures 5 and 6 display the angular distributions of the DDCS at eight different representative energies for He and Ne targets, respectively. The solid line corresponds to the prior form of the CDW-EIS model and the dashed line represents the corresponding post form. For He (Fig. 5), at very low energies such as 3 eV the angular distribution is nearly flat. This means that these low-energy

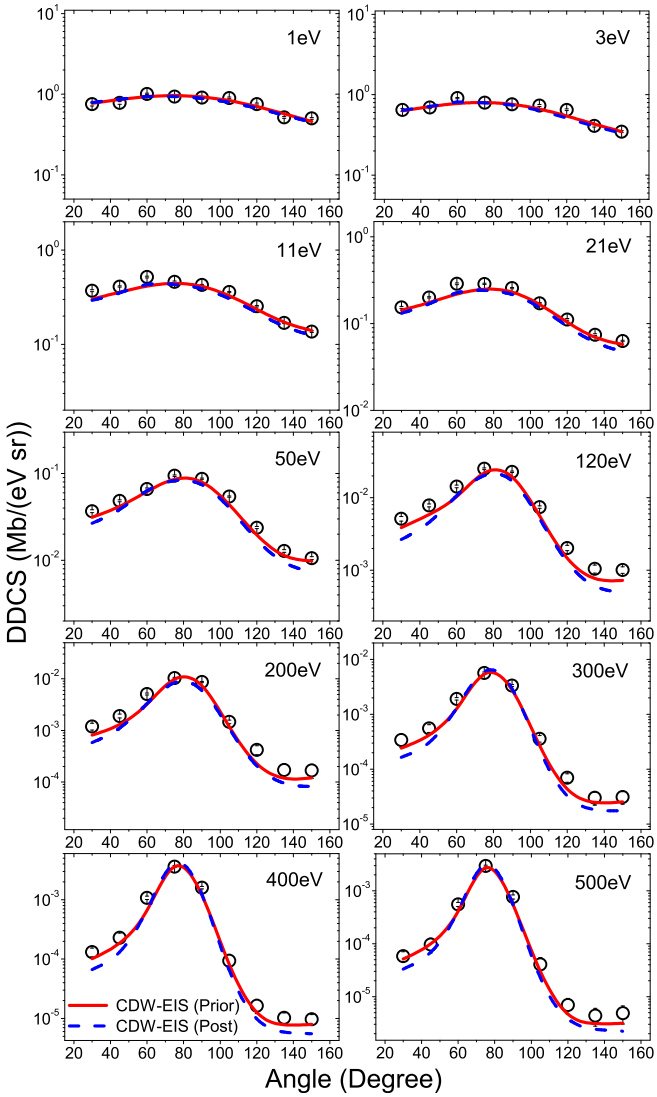

FIG. 5. (Color online) Angular distributions of the DDCS at fixed emission energies for He. Solid (dashed) lines represent CDW-EIS prior (post) form.

electrons are nearly isotropically scattered. These are mainly influenced by the target nucleus; as a result the distribution becomes isotropic. As the energy increases, a sharp peak at around 80° is being noticed. This difference in the shape (peak structure) of the distribution with the variation of electron energy has been discussed earlier in the context of binary encounter collision [16]. It can be noticed from the figures (Fig. 5) corresponding to the high energy electrons (21 eV onwards) that the distributions are not symmetric about the peak, i.e., the cross section at forward angles are larger than the backward angles. In the case of 21 eV, the ratio of DDCS at 30° to that of 150° is about 2.4, whereas for 500 eV this ratio is about 12.0. Clearly, it suggests that the ratio between the DDCS at the extreme forward angle and that of the extreme backward angle increases with the increase in electron energy. This large forward-backward angular asymmetry can be explained in terms of the two-center effects (TCE). Due to the Coulomb attraction of the forward moving highly charged projectile, the electrons are dragged in the forward direction

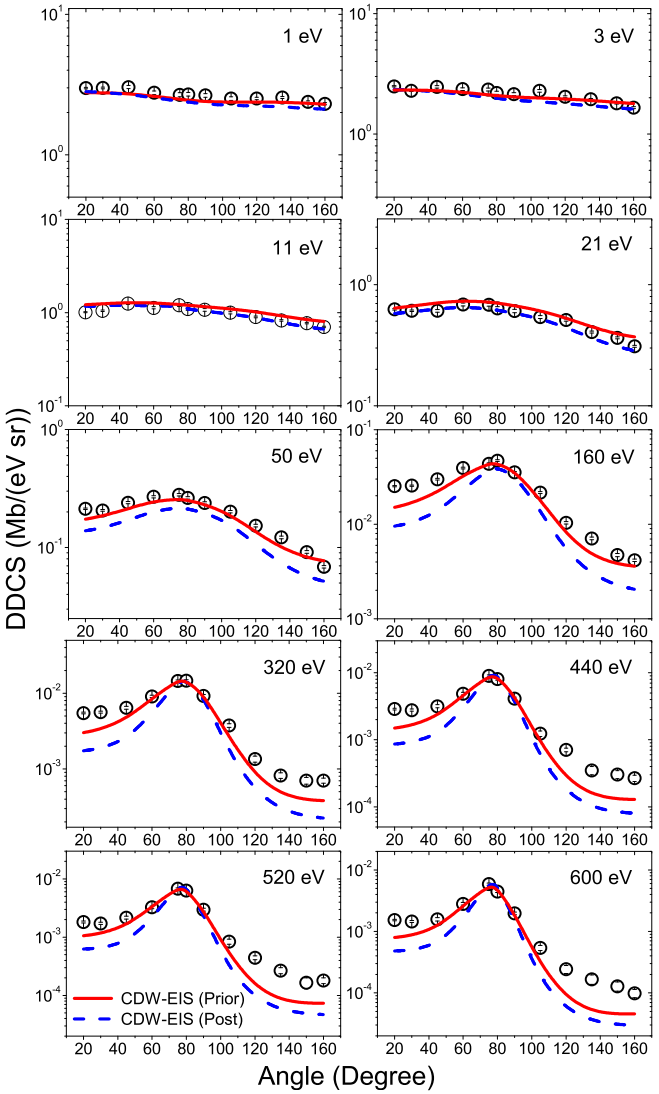

FIG. 6. (Color online) Same as Fig. 5 for Ne target.

which causes the enhancement in the cross section in the forward direction. Low-energy electrons are relatively less affected by the TCE compared to the high-energy electrons, because their velocities are less comparable to the velocity of the projectile ion. As a result, the angular distributions for high-energy electrons are much more asymmetric compared to those for low-energy electrons. Similar observations were reported earlier in Refs. [1,15].

In general, the angular distribution spectra for He (Fig. 5) are very well reproduced by the CDW-EIS model of both the forms. But very close inspection suggests that there are small discrepancies between the experiment and the post form in the extreme forward and the backward angles, at higher energies. On the other hand, the agreement with the prior calculation is excellent for all energies. It should be noticed that the binary encounter peaks at higher energies are well, procreated by both the theoretical calculations, which is expected, because it is purely a two-body collision process and it should be well explained by any quantum mechanical first-order approximation.

In the case of the Ne DDCS angular distribution (Fig. 6), the qualitative behavior of the data is the same as of He. But at lower energies, the distributions are much more flat compared to that for the He. As far as theoretical calculations are concerned, at lower energies (i.e., 3 and 11 eV) both the calculations are matching well with experimental data, though there is slight difference between the two calculations, especially at backward angles. But after that, i.e., 30 eV onwards, the prior calculation is matching relatively better than the post one which underestimates the cross section. This behavior confirms the recent predictions by Monti *et al.* [53] (also see Nandi *et al.* [54]) on the role played by dynamic screening. At higher energies ($\gtrsim$ 300 eV) both the forms of the model are underestimating the DDCS values at the forward and the backward angles. For example, in case of 600 eV at 20°, the prior form underestimates the data by a factor of 1.9, whereas the post form underestimates it by a factor of 3.2. For 150° these values are 2.1 and 3.3, respectively (see Fig. 4). The ratios of DDCS values corresponding to 20° and 160°, as obtained experimentally, are about 2.7 and 15.5 for 50 eV and 600 eV, respectively. These same ratios obtained from the prior and the post calculations are 2.4 and 2.6, respectively, for 50 eV and for 600 eV these are 16.4 and 16.0, respectively. These values along with the experimental ones (given in the second paragraph in this section) suggest that, although there are discrepancies between the experimental and the theoretical absolute DDCS values, the degree of asymmetry observed in the experimental data is well reproduced by the theoretical calculations for all energies.

C. Angular asymmetry parameter

As seen in the above sections, the DDCS angular distribution is asymmetric with respect to the binary encounter peak. In order to quantify this angular asymmetry, we introduce the angular asymmetry parameter $\alpha(k)$ as [21],

$$\alpha(k,\theta) = \frac{\sigma(k,\theta) - \sigma(k,\pi-\theta)}{\sigma(k,\theta) + \sigma(k,\pi-\theta)}, \tag{13}$$

where electron energy $\epsilon_k = \frac{k^2}{2}$ (a.u.) and θ is the extreme forward angle. Since angular distribution varies slowly near 0 and π, we have used measured DDCS at $\theta = 30°$ to approximately calculate the $\alpha(k,\theta)$ as the forward-backward angular asymmetry. Figure 7 shows the ejected electron velocity dependence of the angular asymmetry parameter for He (a) and Ne (b). It may be seen from both the plots that $\alpha(k,\theta)$ is small in the low-velocity limit and then increases nonlinearly with the velocity, which means that the high-velocity electrons are scattered relatively more asymmetrically. This is because the high-energy electrons have velocity closer to the projectile relative to the low-energy electrons; as a result the influence of projectile Coulomb field is relatively higher on the high-energy electrons. In this context, it is worth mentioning that, earlier, similar enhancement of asymmetry with electron energy was also referred to pure kinematic effect [55].

In the case of He [Fig. 7 (a)], the $\alpha(k,\theta)$ parameter varies from 0.2 to 0.8 over an energy range of 1 to 500 eV. In the low-velocity side from $v = 1$ a.u. to about $v = 4.5$ a.u post form of the theory is going slightly higher than the prior form and it is matching with the data well. After that both the theories are

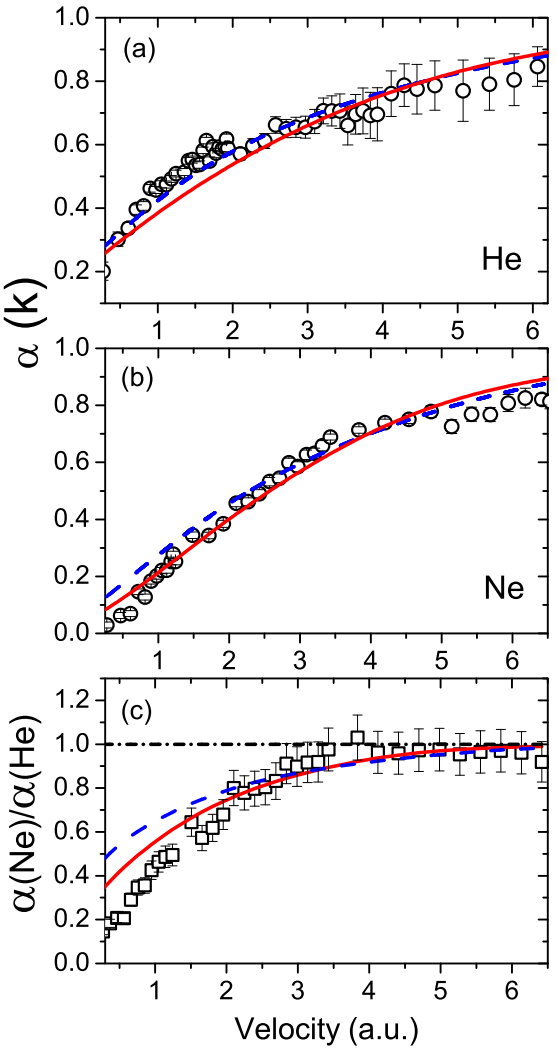

FIG. 7. (Color online) Ejected electron velocity dependence of angular asymmetry parameter (α) for He (a) and Ne (b). In (c), velocity distribution of the ratio of αs corresponding to Ne and He is displayed. Solid (dash) lines represent prior (post) form. Dash dot line in (c) is ratio = 1.

going together and remain within the statistical uncertainty of the data points.

For Ne [Fig. 7 (b)], the $\alpha(k,\theta)$ parameter varies from 0.1 to 0.8 over an energy range of 1 to 600 eV. Here the prior version of the theory is matching very well right from the low velocity. Post form overestimates the experimental observation in the low-velocity region. After $v = 5.5$ a.u. there is a slight mismatch between data and both the forms of theory. Earlier, a large ($\backsim$0.6) forward-backward asymmetry was reported for low-energy electrons ($\epsilon \leqslant 10$) in the 106-keV p + Ne collision [21,31], which was assumed to be due to the two-center effect (TCE). However, there was a large discrepancy between the experimentally observed $\alpha(k,\theta)$ and that from the CDW-EIS calculation [21]. In the present case, the observed small asymmetry in the low-energy limit is well supported by the CDW-EIS model.

Another interesting aspect is the comparison between the asymmetry parameter [$\alpha(k,\theta)$] for He and Ne. In Fig. 7(c), the ratio, α(Ne)/α(He), is plotted against the ejected electron velocity. It shows that at low velocity the ratio is much less than one, i.e., the asymmetry for Ne is much less than that in the case of He. Then it gradually increases with velocity. After about 3 a.u. the ratio becomes 1.0 and continues to be 1.0 for higher velocities. As far as theoretical models are concerned, both the forms are expecting the same qualitative behavior as of experiment, although the prior form (solid line) has better agreement at low velocities. In Ref. [21], qualitatively same behavior was predicted, where the B1 calculation was carried out along with the CDW-EIS calculation for different targets. These calculations show that the difference in the value of α for He and Ne, at low velocities is mainly due to the intrinsic non-Coulombic part of the target potentials. TCE gives rise to some additional unidirectional (forward electron emission enhancement) asymmetry on top of that.

D. Angular distribution of Auger (Ne) yield

After inner-shell ionization or inner-shell electron transfer during collision, the target atom relaxes via electron emission or characteristic x-ray emission. For the systems like the present one, electron emission by the Auger process is a much more favorable process than the x-ray emission. In Fig. 8, the absolute Auger yields are plotted as a function of observation angle. It shows a nearly flat distribution (within the uncertainty) with a very small negative slope (-0.0003). The ground state of the Ne atom is $^1S_0$. When the atom is K-shell ionized by ion impact, it emits Auger electron following the de-excitation of the initial states with the angular momentum of $J \geqslant \frac{1}{2}$. Those electrons, which come from the state $J = \frac{1}{2}$, would have an isotropic angular distribution, whereas the angular distribution of electrons coming following the decay of the initial state $J > \frac{1}{2}$ is anisotropic in nature [56–58]. This anisotropy is caused due to the fact that the magnetic sublevels corresponding to the $J > \frac{1}{2}$ states are not equally populated by quantization with respect to the ion beam direction. In case of light ion impact, the number of initial states formed with $J > \frac{1}{2}$ are not many. As a result of that, the angular distribution remains isotropic in nature. On the other hand, heavy ion impact causes a considerable number of K-shell ionizations along with L-shell ionization or excitation, which causes the $J > \frac{1}{2}$ initial state, resulting in anisotropic angular distribution. Therefore, the present observation of

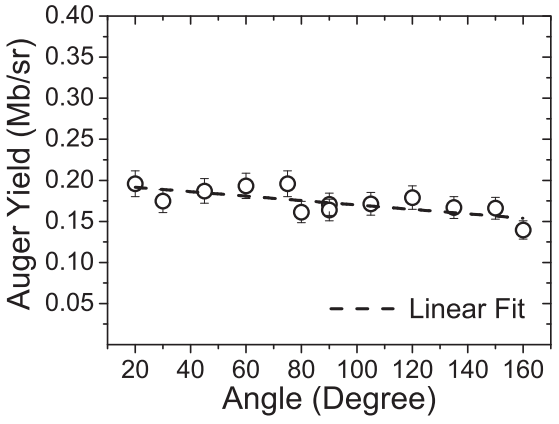

FIG. 8. Angular distribution of Auger electron SDCS for Ne.

slight angular asymmetry is the indication of multiple *L*-shell vacancies along with *K*-shell ionization. It is worth mentioning that, earlier, similar observations were reported by other groups also [59,60].

From the angular distribution, we have deduced the total Auger cross section for Ne and it comes out to be 2.2 Mb. It is also compared with the ECPSSR model [61,62], which gives the value as 2.9 Mb. These studies well compliment the studies using the *K* x-ray detection technique [63] to some extent.

E. Single differential cross sections (SDCS)

To understand the overall angular and energy distribution of electrons emitted in the collisions, the SDCS has been derived by integrating the DDCS spectrum. Figure 9(a) displays the absolute electron SDCS spectra as a function of emission angle, whereas Fig. 9(b) shows the SDCS as a function of energy for both the targets. The SDCS in angle ($\frac{d\sigma}{d\Omega_e}$) is obtained by integrating the DDCS over the electron energy ϵ_e as

$$\frac{d\sigma}{d\Omega_e} = \int_{\epsilon_i}^{\epsilon_f} \frac{d^2\sigma}{d\Omega_e d\epsilon_e} d\epsilon_e. \tag{14}$$

Similarly, the SDCS in ejected energy ($\frac{d\sigma}{d\epsilon_e}$) is obtained by integrating DDCS over the solid angle of emission Ω_e,

$$\frac{d\sigma}{d\epsilon_e} = \int_{\theta_i}^{\theta_f} \frac{d^2\sigma}{d\Omega_e d\epsilon_e} d\Omega_e. \tag{15}$$

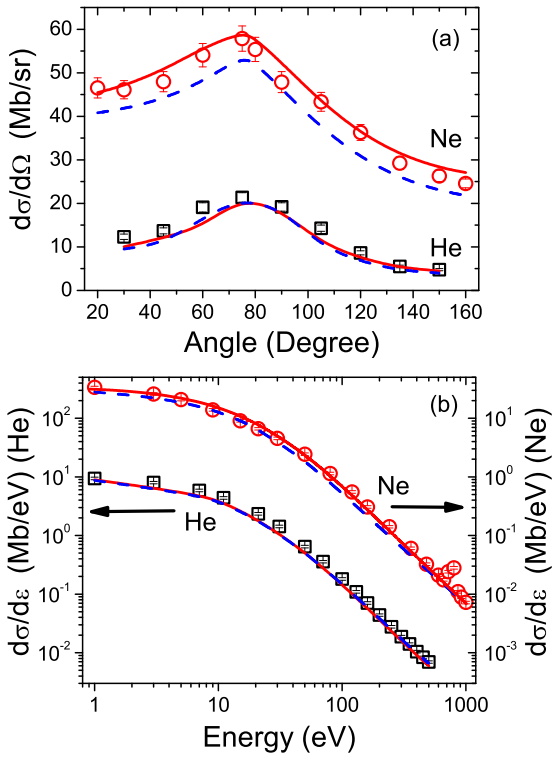

FIG. 9. (Color online) Absolute electron SDCS as a function of emission angle (a) and electron energy (b). In both graphs the upper set of plots corresponds to Ne and the lower one corresponds to He. (b) Left vertical scale is for He and right vertical scale is for Ne. Solid (dashed) lines represent prior (post) form calculation.

In angular distribution plots [Fig. 9(a)], the integration limits have been taken as 1 eV and 500 eV for He and 1 eV and 1000 eV for Ne. For He, the angular distribution of SDCS is qualitatively reproduced by both prior (solid line) and post (dashed line) forms of the theory. In forward angles both the forms are underestimating the data slightly, whereas in backward angles the prior form has better agreement than the post one. In the case of Ne, the post (dashed line) version is underestimating the data for most of the data points and the prior (solid line) form has a much better agreement. Unlike He, in this case, the post form is going below the prior calculation throughout the entire angular range. It is a further indication that dynamic screening plays an important role in the case of multielectronic atomic targets. It should be mentioned that the origin of the humplike structure around 80° is due to the binary nature of the collision.

For obtaining the SDCS in energy ($\frac{d\sigma}{d\epsilon_e}$) values [Fig. 9(b)], the DDCS values have been integrated over an angular range of 30° to 150° for He and 20° to 160° for Ne. The contributions from extreme forward angle and backward angles (e.g., less than 20° and greater than 160° for Ne) were small as estimated by extrapolating. A fairly good qualitative agreement among both the forms of the theory and experiment have been observed in the case of He. For the Ne target, the prior (solid line) version is matching very well throughout the spectrum, whereas the post (dashed line) form is underestimating both the prior form as well as the data points. The Auger peak at 780 eV is also clearly visible in the SDCS spectrum.

The total cross section (TCS) obtained from the experimental data for He is about 170 Mb, whereas the TCS obtained from the prior and the post forms of the theoretical calculation are about 151 Mb and 148 Mb, respectively. Evidently, the theoretical values underestimate the experimental value by an approximate factor of about 1.1. In the case of Ne, the experimentally obtained TCS value is 511 Mb. This value is given as 541 Mb and 467 Mb by the prior and the post forms, respectively. Therefore, the prior calculation is overestimating the data by a factor of 1.05, whereas the post form underestimates the data by a factor of 1.1.

V. CONCLUSION

In conclusion, we have reported the absolute double-differential cross sections of electron emission as a function of electron energy and ejection angle, in ionization of He and Ne atoms under the impact of 6 MeV/u bare carbon ions. A stringent test has been provided to the post and the prior versions of the CDW-EIS model in the case of multielectronic systems. For He, the discrepancy between these two theoretical versions is relatively small. The prior form reproduces the experimental findings very well, whereas the post form is slightly underestimating the data especially in the extreme forward and the backward angles. In the case of Ne, a substantial discrepancy has been seen between both the theoretical versions. Almost for all angles, in the low-energy region both the forms agree well with the experimental data. But at higher energies ($\gtrsim$35 eV) and in extreme forward and backward angles, these are underestimating the data, although the prior version has much better agreement compared to the post version. This post-prior discrepancy as well as the larger

deviation of theoretical models from experimental observations, especially in the case of Ne, suggest the importance of the dynamic screening effect introduced by the target passive electrons. To reduce the difference between the experimental observation and the theoretical prediction, proper inclusion of the dynamic screening effect in the CDW-EIS framework is needed. The single differential cross sections for both the targets obtained by integrating the DDCS are also in overall good quantitative agreement with the theoretical predictions. The absolute total ionization cross sections were found to be 170 and 511 Mb for He and Ne, respectively. These values match quite well with the theoretically calculated values. In the case of the Ne target, the angular distribution of absolute differential Auger yield is also presented here. It shows slightly asymmetric distribution, which may be due to the multiple vacancies in the L shell along with the K-shell vacancy. The total Auger yield is calculated from the angular distribution and it comes out to be 2.2 Mb. This value is also compared with the ECPSSR model, which gives a slightly higher value. In addition to that a detailed discussion on the forward-backward angular asymmetry in electron emission has also been presented. This shows lower value of the asymmetry parameter in the case of Ne compared to He, for lower electron velocities. After certain velocity ($\gtrsim$ 3 a.u.), a similar degree of asymmetry is observed for both the targets. All these observations are excellently supported by the theoretical calculations.

ACKNOWLEDGMENTS

The authors would like to thank A. N. Agnigotri, S. Kasthurirangan, S. Nandi, and A. Khan for their help during the experiment and the staffs at BARC-TIFR Pelletron accelerator facility for smooth operation of the machine.

[1] N. Stolterfoht, R. D. DuBois, and R. D. Rivarola, *Electron Emission in Heavy Ion-Atom Collisions* (Springer-Verlag, Berlin, 1997).
[2] C. E. Kuyatt and T. Jorgenson, Jr., Phys. Rev. **130**, 1444 (1963).
[3] Lokesh C. Tribedi, P. Richard, L. Gulýas, and M. E. Rudd, Phys. Rev. A **63**, 062724 (2001).
[4] D. Misra, U. Kadhane, Y. P. Singh, Lokesh C. Tribedi, P. D. Fainstein, and P. Richard, Phys. Rev. Lett. **92**, 153201 (2004).
[5] Lokesh C. Tribedi, P. Richard, Y. D. Wang, C. D. Lin, and R. E. Olson, Phys. Rev. Lett. **77**, 3767 (1996).
[6] N. Stolterfoht, B. Sulik, V. Hoffmann, B. Skogvall, J. Y. Chesnel, J. Rangama, F. Frémont, D. Hennecart, A. Cassimi, X. Husson, A. L. Landers, J. A. Tanis, M. E. Galassi, and R. D. Rivarola, Phys. Rev. Lett. **87**, 023201 (2001).
[7] J. A. Tanis, S. Hossain, B. Sulik, and N. Stolterfoht, Phys. Rev. Lett. **95**, 079301 (2005).
[8] Deepankar Misra, A. Kelkar, U. Kadhane, Ajay Kumar, Lokesh C. Tribedi, and P. D. Fainstein, Phys. Rev. A **74**, 060701(R) (2006).
[9] J. A. Tanis, J. Y. Chesnel, B. Sulik, B. Skogvall, P. Sobocinski, A. Cassimi, J. P. Grandin, L. Adoui, D. Hennecart, and N. Stolterfoht, Phys. Rev. A **74**, 022707 (2006).
[10] Deepankar Misra, A. H. Kelkar, S. Chatterjee, and Lokesh C. Tribedi, Phys. Rev. A **80**, 062701 (2009).
[11] Shyamal Chatterjee, D. Misra, A. H. Kelkar, Lokesh C. Tribedi, C. R. Stia, O. A. Fojón, and R. D. Rivarola, Phys. Rev. A **78**, 052701 (2008).
[12] Lokesh C. Tribedi, P. Richard, Y. D. Wang, C. D. Lin, L. Gulýas, and M. E. Rudd, Phys. Rev. A **58**, 3619 (1998).
[13] F. Frémont, A. Hajaji, A. Naja, C. Leclercq, J. Soret, J. A. Tanis, B. Sulik, and J. Y. Chesnel, Phys. Rev. A **72**, 050704(R) (2005).
[14] N. Stolterfoht, D. Schneider, J. Tanis, H. Altevogt, A. Salin, P. D. Fainstein, R. D. Rivarola, J. P. Grandin, J. N. Scheurer, S. Andriamonje, D. Bertault, and J. F. Chemin, Europhys. Lett. **4**, 899 (1987).
[15] N. Stolterfoht, H. Platten, G. Schiwietz, D. Schneider, L. Gulýas, P. D. Fainstein, and A. Salin, Phys. Rev. A **52**, 3796 (1995).
[16] Steven T. Manson, L. H. Toburen, and N. Stolterfoht, Phys. Rev. A **12**, 60 (1975).
[17] D. S. F. Crothers and J. F. McCann, J. Phys. B: At. Mol. Opt. Phys. **16**, 3229 (1983).
[18] I. M. Cheshire, Proc. R. Phys. Soc. (London) **84**, 89 (1964).
[19] Dz. Belkić, J. Phys. B: At. Mol. Opt. Phys. **11**, 3529 (1978).
[20] P. D. Fainstein, V. H. Ponce, and R. D. Rivarola, J. Phys. B: At. Mol. Opt. Phys. **21**, 287 (1988).
[21] P. D. Fainstein, L. Gulýas, F. Martin, and A. Salin, Phys. Rev. A **53**, 3243 (1996).
[22] T. Kirchner and M. Horbatsch, Phys. Rev. A **63**, 062718 (2001).
[23] S. Yu. Ovchinnikov, D. B. Khrebtukov, and J. H. Macek, Phys. Rev. A **65**, 032722 (2002).
[24] H. J. Lüdde, T. Spranger, M. Horbatsch, and T. Kirchner, Phys. Rev. A **80**, 060702(R) (2009).
[25] J. Colgan and M. S. Pindzola, Eur. Phys. J. D **66**, 284 (2012).
[26] H. R. J. Walters and C. T. Whelan, Phys. Rev. A **85**, 062701 (2012).
[27] M. F. Ciappina, M. S. Pindzola, and J. Colgan, J. Phys. B: At. Mol. Opt. Phys. **46**, 215206 (2013).
[28] T. Kirchner and Helge Knudsen, J. Phys. B: At. Mol. Opt. Phys. **44**, 122001 (2011).
[29] F. Wang, X. H. Hong, J. Wang, B. C. Gou, and J. G. Wang, Phys. Lett. A **376**, 469 (2012).
[30] M. Baxter and T. Kirchner, Phys. Rev. A **87**, 062507 (2013).
[31] S. Suaŕez, C. Garibotti, W. Meckbach, and G. Bernardi, Phys. Rev. Lett. **70**, 418 (1993).
[32] S. Suaŕez, C. Garibotti, G. Bernardi, P. Focke, and W. Meckbach, Phys. Rev. A **48**, 4339 (1993).
[33] J. B. Crooks and M. E. Rudd, Phys. Rev. A **3**, 1628 (1971).
[34] Wen-qin Cheng, M. E. Rudd, and Ying-Yuan Hsu, Phys. Rev. A **39**, 2359 (1989).
[35] G. Bernardit, P. Fainstein, C. R. Garibottii, and S. Suárez, J. Phys. B: At. Mol. Opt. Phys. **23**, L139 (1990).
[36] T. J. Gay, M. W. Gealy, and M. E. Rudd, J. Phys. B: At. Mol. Opt. Phys. **23**, L823 (1990).
[37] R. D. DuBois and Steven T. Manson, Phys. Rev. A **42**, 1222 (1990).
[38] R. K. Cacak and T. Jorgensen, Jr., Phys. Rev. A **2**, 1322 (1970).
[39] P. H. Woerleet, Yu S. Gordeev, H. de Waard, and F. W. Saris, J. Phys. B: At. Mol. Opt. Phys. **14**, 527 (1981).

[40] R. Moshammer, J. Ullrich, H. Kollmus, W. Schmitt, M. Unverzagt, H. Schmidt-Böcking, C. J. Wood, and R. E. Olson, Phys. Rev. A **56**, 1351 (1997).
[41] J. Ullrich, R. Moshammer, R. Dörner, O. Jagutzki, V. Mergel, H. Schmidt-Böcking, and L. Spielberger, J. Phys. B: At. Mol. Opt. Phys. **30**, 2917 (1997).
[42] R. Dörner, V. Mergel, O. Jagutzki, L. Spielberger, J. Ullrich, R. Moshammer, and H. Schmidt-Böcking, Physics Reports **330**, 95 (2000).
[43] M. Schulz, R. Moshammer, D. Fischer, H. Kollmus, D. H. Madison, S. Jones, and J. Ullrich, (London) Nature **422**, 48 (2003).
[44] N. V. Maydanyuk, A. Hasan, M. Foster, B. Tooke, E. Nanni, D. H. Madison, and M. Schulz, Phys. Rev. Lett. **94**, 243201 (2005).
[45] M. Dürr, C. Dimopoulou, B. Najjari, A. Dorn, K. Bartschat, I. Bray, D. V. Fursa, Zhangjin Chen, D. H. Madison, and J. Ullrich, Phys. Rev. A **77**, 032717 (2008).
[46] M. Schulz, Phys. Scr. **80**, 068101 (2009).
[47] V. D. Rodríguez, Y. D. Wang, and C. D. Lin, Phys. Rev. A **52**, R9(R) (1995).
[48] Y. D. Wang, L. C. Tribedi, P. Richard, C. L. Cocke, V. D. Rodríguez, and C. D. Lin, J. Phys. B: At. Mol. Opt. Phys. **29**, L203 (1996).
[49] D. Misra, K. V. Thulasiram, W. Fernandes, A. H. Kelkar, U. Kadhane, A. Kumar, Y. P. Singh, L. Gulýas, and L. C. Tribedi, Nucl. Instrum. Methods Phys. Res., Sect. B **267**, 157 (2009).
[50] C. Clementi and C. Roetti, At. Data Nucl. Data Tables **14**, 177 (1974).
[51] J. M. Monti, O. A. Fojón, J. Hanssen, and R. D. Rivarola, J. Phys. B: At. Mol. Opt. Phys. **43**, 205203 (2010).
[52] J. M. Monti, O. A. Fojón, J. Hanssen, and R. D. Rivarola, J. At. Mol. Opt. Phys. **2010**, 1 (2010).
[53] J. M. Monti, O. A. Fojón, J. Hanssen, and R. D. Rivarola, J. Phys. B: At. Mol. Opt. Phys. **46**, 145201 (2013).
[54] S. Nandi, S. Biswas, A. Khan, J. M. Monti, C. A. Tachino, R. D. Rivarola, D. Misra, and L. C. Tribedi, Phys. Rev. A **87**, 052710 (2013).
[55] R. Moshammer, J. Ullrich, M. Unverzagt, W. Schmidt, P. Jardin, R. E. Olson, R. Mann, R. Dörner, V. Mergel, U. Buck, and H. Schmidt-Böcking, Phys. Rev. Lett. **73**, 3371 (1994).
[56] B. Cleff and W. Mehlhorn, J. Phys. B: At. Mol. Opt. Phys. **7**, 593 (1974).
[57] B. Cleff and W. Mehlhorn, J. Phys. B: At. Mol. Opt. Phys. **7**, 605 (1974).
[58] Ajay Kumar, A. N. Agnihotri, D. Misra, S. Kasthurirangan, L. Sarkadi, and L. C. Tribedi, J. Phys. B: At. Mol. Opt. Phys. **45**, 215205 (2012).
[59] N. Stolterfoht, D. Schneider, D. Burch, B. Aagaard, E. Bøving, and B. Fastrup, Phys. Rev. A **12**, 1313 (1975).
[60] N. Kobayashi, T. Irie, N. Maede, H. Kojima, S. Akanuma, and M. Sakisaka, J. Phys. Soc. Jpn. **47**, 234 (1979).
[61] W. Brandt and G. Lapicki, Phys. Rev. A **23**, 1717 (1981).
[62] G. Lapicki, M. Goldstein, and W. Brandt, Phys. Rev. A **23**, 2727 (1981).
[63] L. C. Tribedi and P. N. Tandon, Nucl. Instrum. Methods Phys. Res., Sect. B **69**, 178 (1992).